Journal of Materials Chemistry A

PAPER

View Article Online
View Journal | View Issue

Cite this: J. Mater. Chem. A, 2015, 3, 8840

Nitrogen and sulfur co-doped porous carbon derived from human hair as highly efficient metal-free electrocatalysts for hydrogen evolution reactions†

Xiaojun Liu,[a] Weijia Zhou,*[a] Linjing Yang,[a] Ligui Li,[a] Zhenyuan Zhang,[a] Yunting Ke[a] and Shaowei Chen*[ab]

Received 13th February 2015
Accepted 19th March 2015

DOI: 10.1039/c5ta01209k

www.rsc.org/MaterialsA

Design and engineering of low-cost and high-efficiency electrocatalysts for hydrogen evolution reactions (HER) has attracted increasing interest in renewable energy research. Herein, a highly active and stable metal-free electrocatalyst, N and S co-doped porous carbon derived from human hair, was developed for HER for the first time, with an electrocatalytic performance comparable to that of state-of-the-art commercial 20 wt% Pt/C catalysts. SEM, TEM and nitrogen adsorption–desorption measurements showed that the resultant carbon exhibited a porous structure with a high specific surface area (up to 830.0 m^2 g^{-1}) and rich porosity. XPS measurements showed that N and S were co-doped into the carbon molecular skeletons. Importantly, electrochemical measurements showed high activity for hydrogen evolution with a low overpotential of only −12 mV, a Tafel slope of 57.4 mV dec^{-1}, a current density of 10 mA cm^{-2} at −0.1 V *vs.* RHE, and remarkable durability. The results highlight a unique paradigm for the preparation of highly efficient electrocatalysts for HER based on abundant biowastes.

Introduction

Increasing global concerns over environmental issues and energy crisis have stimulated a great deal of interest in the development of novel technologies for clean and sustainable energy. Hydrogen has been widely considered as a promising fuel to address the environmental and energy concerns, mainly due to its high heat of combustion and high energy capacity per unit volume, as compared to conventional fossil fuels. In addition, the combustion of hydrogen is pollution-free, generating only water as the product. Therefore, hydrogen evolution reaction (HER), the electrochemical reduction of water, has been attracting extensive attention lately.[1,2] Currently, Pt-group metals are the most effective catalysts for HER; yet large-scale applications have been hampered by high costs and limited reserves.[3] Thus, the development of HER electrocatalysts composed of cost-effective and earth-abundant elements with high catalytic activity and stability is crucial in renewable energy research. Towards this end, Mo-based sulfides, nitrides, carbides (*e.g.*, MoS_2, Mo_2C and Ni–Mo–N),[4–9] Co/Ni-based metal sulfides, selenides, phosphides (*e.g.*, CoS_2, $CoSe_2$, CoP, and $Ni_{12}P_5$)[10–13] and Co-embedded nitrogen-rich carbon[14–17] have been prepared and examined as effective HER catalysts in a series of recent studies.

In more recent research, carbon-based nanomaterials have also been found to serve as a new class of effective HER catalysts. For instance, Qiao[18] and Wang[19] independently reported that g-C_3N_4 loaded on N-doped graphene exhibited unexpected electrocatalytic activity for HER with an overpotential and Tafel slope comparable to those of well-developed metallic catalysts. Yet, the activity of carbon itself has been reported to be relatively low and thus largely ignored in the research community. Interestingly, by the incorporation of heteroatoms, such as nitrogen, phosphorus or sulfur, into the carbon frameworks, it has been found that the electrocatalytic activities towards HER can be significantly enhanced.[20–25] For instance, Chen *et al.*[20] reported that nitrogen and sulfur co-doped nanoporous graphene displayed high catalytic activity in HER that was comparable to that of the best Pt-free MoS_2 catalysts. However, the synthetic process was rather expensive, complex, and tedious, involving the preparation of nanoporous Ni substrates and nanoporous graphene by the CVD method. In fact, reports of carbon nanostructures as non-metal HER catalysts have been rather scarce, where a deep understanding of the HER mechanism for carbon-based electrocatalysts is urgently needed. This is the primary motivation of the present work.

[a]New Energy Research Institute, School of Environment and Energy, South China University of Technology, Guangzhou Higher Education Mega Center, Guangzhou, Guangdong 510006, China. E-mail: eszhouwj@scut.edu.cn

[b]Department of Chemistry and Biochemistry, University of California, 1156 High Street, Santa Cruz, California 95064, USA. E-mail: Shaowei@ucsc.edu

† Electronic supplementary information (ESI) available: Additional experimental data and discussion, video S1, Tables S1, S2 and Fig. S1–S9. See DOI: 10.1039/c5ta01209k

Whereas carbon nanomaterials may be prepared from a variety of abundant biomass materials,[26–28] to date, no studies have been reported on biomass-derived doped carbon catalysts for HER. Therefore, in the present study, we describe a facile experimental procedure where human hair was used as the source material to prepare porous carbons that were co-doped with S and N, by taking advantage of the rich elemental nature of the hair. Note that N and S self-doped porous carbons have been derived from human hair and used as electrode materials for electrochemical supercapacitors[29,30] and as metal-free catalysts for the oxygen reduction reaction (ORR),[31] but not for HER thus far, to the best of our knowledge. Herein, for the first time, we demonstrated that HER might be effectively catalyzed by N and S self-doped porous carbons derived from human hair. XPS measurements showed that both N and S were incorporated into the carbon scaffolds. Nitrogen adsorption–desorption measurements showed that the porous carbons exhibited a high specific surface area (up to 830.0 $m^2 g^{-1}$) and rich porosity. Electrochemical studies showed that the porous carbons exhibited high catalytic activity and stability for HER, with an onset potential of only −0.012 V *vs.* RHE, a Tafel slope of 57.4 mV dec^{-1} and remarkable durability, as compared to state-of-the-art commercial 20 wt% Pt/C catalysts.

Experimental section

Chemicals

$ZnCl_2$ (98.0%) was purchased from Damao Company (Tianjin). Nafion solution (5%) and commercial Pt/C (20 wt%) were purchased from Alfa Aesar. All reagents were used without further purification. Water was supplied with a Barnstead Nanopure Water Purification System (18.3 MΩ cm).

Preparation of porous carbon from human hair

Hair was collected from the lead author and used as the precursor. In a typical synthetic procedure, the hair was first ultrasonically washed with acetone, alcohol and deionized water, and dried under vacuum at 80 °C for 12 h. The cleaned hair was then cut into small pieces, and pre-carbonized at 300 °C for 1.5 h under a nitrogen atmosphere. The resulting sample was chemically activated by heating again with $ZnCl_2$ under N_2 at elevated temperatures (600–900 °C) for 2 h at a heating rate of 5 °C min^{-1}, where $ZnCl_2$ was used as an activation agent to produce high porosity and high specific surface area.[32,33] To remove inorganic salts, the final products were first washed with 2 M HCl, and then with distilled water until the pH value of the filtrate reached 7.0. Finally, the sample was dried under vacuum at 80 °C for 12 h, affording human hair-derived porous carbons which were denoted as HPC-T (with T being the temperature at which the sample was prepared).

Characterization

The morphology was examined with a field-emission scanning electron microscope (FESEM, Zeiss) and a high-resolution transmission electron microscope (HRTEM, JEOL JEM-2010). X-ray powder diffraction (XRD) patterns in the Bragg's angle (2θ) range of 10 to 80° were collected at room temperature using a Bruker D_8 diffractometer with Cu K_α radiation ($\lambda = 0.1541$ nm). Raman measurements were run on a LabRAM HR Evolution system equipped with a deep-depleted thermoelectrically cooled CCD array detector, an Ar laser (514.5 nm) and long working distance 50× objective lens. N_2 adsorption analysis was conducted on an ASAP 2020 accelerated surface area and porosimetry instrument (Micromeritics) at 77 K using Barrett–Emmett–Teller (BET) calculations for the quantification of specific surface areas. Pore size distribution (PSD) was calculated *via* a density function theory (DFT) method by using nitrogen adsorption data and assuming a slit pore model.[34] X-ray photoelectron spectroscopy (XPS) was carried out with a SPECS spectrometer, using Mg K_α (1253.6 eV) radiation from a double anode at 150 W. Binding energies for the high resolution spectra were calibrated by setting C 1s to 284.6 eV.

Electrochemistry

Electrochemical measurements were performed with an electrochemical workstation (CHI 760C, CH Instruments Inc.) in a 0.5 M H_2SO_4 aqueous solution. An Ag/AgCl electrode (saturated KCl) and platinum wire were used as the reference and counter electrodes, respectively. 4 mg of the catalyst powders was dispersed in 1 mL of 4 : 1 (v/v) water–ethanol mixed solvents along with 80 μL of a Nafion solution, and the mixture was sonicated for 30 min. Then, 5 μL of the above solution was drop-cast onto the surface of a glassy carbon (GC) disk electrode at a catalyst loading of 0.285 mg cm^{-2}. The catalyst film was dried at room temperature. Polarization curves were acquired by sweeping the potential between 0 and −0.8 V (*vs.* Ag/AgCl) at a potential sweep rate of 5 mV s^{-1}. Accelerated stability tests were performed in 0.5 M H_2SO_4 at room temperature by potential cycling between 0 and −0.6 V (*vs.* Ag/AgCl) at a sweep rate of 100 mV s^{-1} for a given number of cycles. Current–time responses were monitored by chronoamperometric measurements for 12 h. The obtained gas product was confirmed to be H_2 by gas chromatographic measurements.

In all measurements, the Ag/AgCl reference electrode was calibrated with respect to a reversible hydrogen electrode (RHE). The calibration was performed in a high-purity H_2 (99.999%) saturated electrolyte with Pt wire as the working electrode and counter electrode. Cyclic voltammograms were collected at a scan rate of 1 mV s^{-1}, and the average of the two potentials at which the current crossed zero was taken as the thermodynamic potential for the hydrogen electrode reactions. In 0.5 M H_2SO_4, $E_{Ag/AgCl} = E_{RHE} + 0.273$ V in the present study.

Results and discussion

The morphology and structure of the resulting porous carbons were first examined by SEM measurements. Fig. 1 shows the representative SEM images for the (a) HPC-600, (b) HPC-700, (c) HPC-800, and (d) HPC-900 samples. It can be seen that all four samples exhibited a similar morphology with a rather rough surface and a randomly distributed and yet uniform pore structure. Further structural insights were obtained in TEM

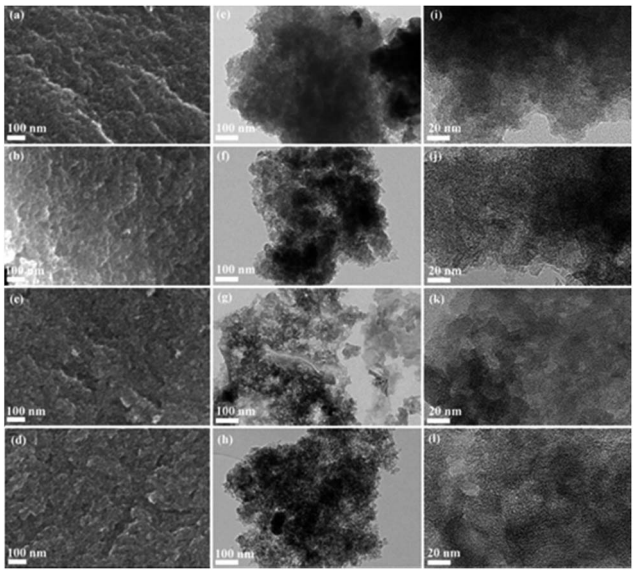

Fig. 1 Representative SEM and TEM images of (a, e, i) HPC-600, (b, f, j) HPC-700, (c, g, k) HPC-800, and (d, h, l) HPC-900. Scale bars are 100 nm in panels (a) to (h) and 20 nm in panels (i) to (l).

measurements, as depicted in panels (e) to (l), where all samples were found to consist of a number of stacked nanosheets with a highly porous structure.

The structures of the porous carbons were then studied by XRD measurements (Fig. 2a). All samples exhibited two major diffraction peaks at *ca.* $2\theta = 24.7^\circ$ and 44.0° that might be assigned to the (002) and (101) diffraction planes of hexagonal graphite (JCPDS no. 41-1487), respectively.[35] A closer inspection shows that the (002) diffraction peak actually showed a slight increase of the 2θ value with increasing carbonization temperature at 24.20° for HPC-600, 24.80° for HPC-700, 24.87° for HPC-800, and 24.98° for HPC-900. The corresponding *d*-spacings were estimated to be 3.67, 3.59, 3.58 and 3.55 Å, respectively, suggesting an increasing graphitic order in the samples.

Further structural characterization was conducted by Raman measurements. From Fig. 2b it can be seen that all samples exhibited a G band at *ca.* 1600 cm^{-1} and a D band at *ca.* 1350 cm^{-1} (the broader peak centered at about 2700 cm^{-1} is the so-called 2D band) that were characteristic of graphitic carbons.[36] Note that the D band is generally associated with defects, curved sheets and dangling bonds in the carbon structures whereas the G band corresponds to graphitic carbon with a sp^2 electronic configuration,[37] and the ratio of the D to G band intensities (I_D/I_G) may be used to examine the degree of disordering in the graphitic structure. In the present study, the I_D/I_G ratio was 1.31 for HPC-600, 1.17 for HPC-700, 1.07 for HPC-800, and 0.99 for HPC-900, suggesting an increase of the sp^2 graphitic configuration in the porous carbons with increasing carbonization temperature, in good agreement with the XRD results (Fig. 2a).

Nitrogen adsorption–desorption measurements were then carried out to quantify the specific surface area. Fig. 3a depicts the adsorption–desorption isotherms for the series of porous carbons, from which the corresponding pore size distributions (PSD) were derived using the non-local density functional theory (NL-DFT) method and are shown in Fig. 3b. First, one can see from Fig. 3a that all the porous carbons showed a type-IV isotherm with a greater slope at higher relative pressures, which is commonly related to capillary condensation in mesopores. The sharp increase at low pressure ($<0.45P/P_0$) indicates the formation of micropores. A hysteresis loop extending from $P/P_0 = 0.40$ to 0.85 was also observed for these samples, suggesting the coexistence of both micropores and mesopores in the samples. However, for HPC-800 and HPC-900, an obvious tail appeared at $P/P_0 \sim 1.0$, implying the formation of macropores as well within the carbon structures of these two samples.[38,39] Consistent results can be seen in PSD analysis. It can be seen from Fig. 3b that in the microporous (<2 nm) and mesoporous regions (2–15 nm), the four samples exhibited pores with diameters centered around 0.6, 1.1, 3.2 and 7.1 nm (inset to Fig. 3b). However, in the pore diameter range of 15–150 nm, apparent differences can be seen with HPC-800 and HPC-900 as compared with HPC-600 and HPC-700. Specifically, whereas the PSD curves were largely featureless for HPC-600 and HPC-700, HPC-800 exhibited four rather well-defined peaks at 17.4, 37.1, 51.2 and 62.9 nm, indicating the coexistence of hierarchical mesopores and macropores. Similar behaviors can be seen with HPC-900 but with a somewhat lower intensity in mesopores and macropores.

From these measurements, the specific surface areas (S_{BET}) and pore volumes were then quantitatively estimated, with the results summarized in Table S1.† It can be seen that with increasing pyrolysis temperature, the BET surface area exhibited a marked increase from 535.2 m^2 g^{-1} for HPC-600 to

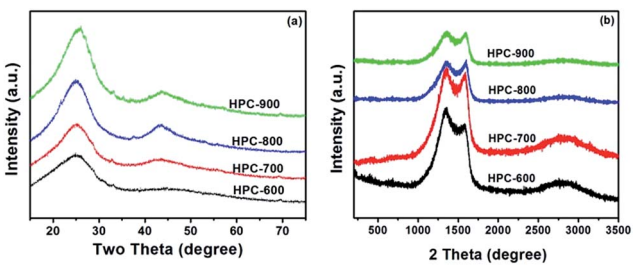

Fig. 2 (a) XRD patterns and (b) Raman spectra of HPC-600, HPC-700, HPC-800 and HPC-900.

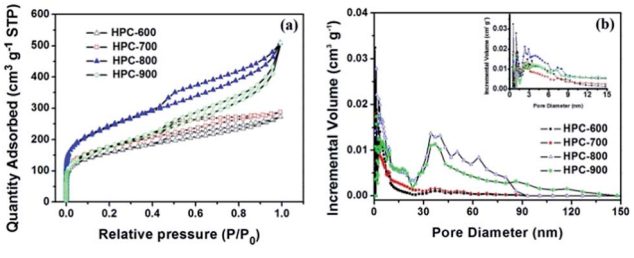

Fig. 3 (a) N_2 adsorption–desorption isotherms and (b) pore-size distributions of HPC-600, HPC-700, HPC-800 and HPC-900. The inset to panel (b) is the zoom-in of the pore-size distributions at pore diameters lower than 15 nm.

597.3 m^2 g^{-1} for HPC-700 and to 830.0 m^2 g^{-1} for HPC-800. However, when the pyrolysis temperature was further increased to 900 °C, the specific surface area was found to decrease to only 617.8 m^2 g^{-1}. A similar trend can be seen with the pore volume which was 0.37, 0.40, 0.88, and 0.65 cm^3 g^{-1}, respectively. This is probably due to the collapse of pores and enhanced graphitization of the carbon frameworks at high temperatures.

Elemental compositions and bonding configurations of the porous carbons were then characterized by XPS measurements. Fig. 4a depicts the survey spectrum of HPC-800 where only the elements of C, N, O and S can be found (the fact that no Zn was identified indicates that it was removed effectively by acid washing). Further analysis was carried out by high-resolution scans of the (b) C 1s, (c) N 1s, and (d) S 2p electrons. From panel (b), deconvolution of the C 1s spectrum yielded three major components, corresponding to C=C (284.7 eV), C–N/C–O/C–S (285.9 eV) and C=O/C=N (288.8 eV). For the N 1s spectrum in Fig. 4c, four subpeaks were deconvoluted at 398.1 eV, 399.8 eV, 401.0 eV, and 401.9 eV corresponding to pyridinic-N, pyrrolic-N, graphitic-N and pyridinic N^+–O^-, respectively.[38,40–42] This suggests that nitrogen was indeed embedded within the skeletons of the porous carbons. Similarly, the S 2p spectrum was found to entail three sulfur moieties (Fig. 4d). The two major peaks at the binding energies of 163.7 and 164.9 eV might be assigned to S 2p in C–S–C and C=S bonds, whereas the pair at 167.9 eV and 169.3 eV most likely arose from the oxidized sulfur species of C–SO_x–C ($x = 2$ or 3),[43–45] indicating that S was also doped into the carbon molecular scaffolds. In comparison, in a previous study[20] where N and S co-doped nanoporous graphene was prepared by nanoporous Ni-based chemical vapour deposition, only three nitrogen dopants were observed (graphitic, pyridinic, and oxide nitrogen), but the sulphur moieties were rather consistent.

The concentrations of the various N and S dopants were then quantified by their integrated peak areas, as shown in Table S2.† Overall, it can be seen that the concentrations of N and S dopants decreased with increasing pyrolysis temperature. For instance, the combined concentration of C–S–C and C=S decreases in the order of 0.58 at% (600 °C) > 0.49 at% (800 °C) > 0.46 at% (700 °C) > 0.41 at% (900 °C). A similar changing trend can be seen with C–SO_x–C (note that these species were absent in the HPC-900 sample, suggesting low stability of C–SO_x–C at high temperatures, Fig. S1†).[20] As for N doping, with an increase of the pyrolysis temperature, the concentrations of pyrrolic and pyridinic nitrogens also decreased, but graphitic nitrogen concentration actually increased, likely because of the enhanced thermal stability of the latter as compared to the former.

Interestingly, the above obtained porous carbons all exhibited apparent electrocatalytic activities for HER. Fig. 5a depicts the polarization curves of a glassy carbon electrode modified with a calculated amount of HPC-600, HPC-700, HPC-800 and HPC-900, along with commercial Pt/C, at the potential scan rate of 5 mV s^{-1} in 0.5 M H_2SO_4. One can see that similar to Pt/C, all porous carbons exhibited nonzero cathodic currents at sufficiently negative electrode potentials. However, the HER activity

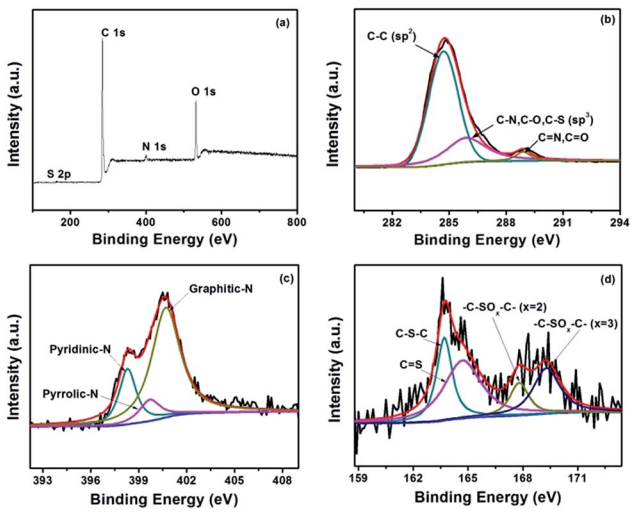

Fig. 4 (a) XPS survey spectrum and high-resolution scans of (b) C 1s, (c) N 1s, and (d) S 2p electrons of HPC-800.

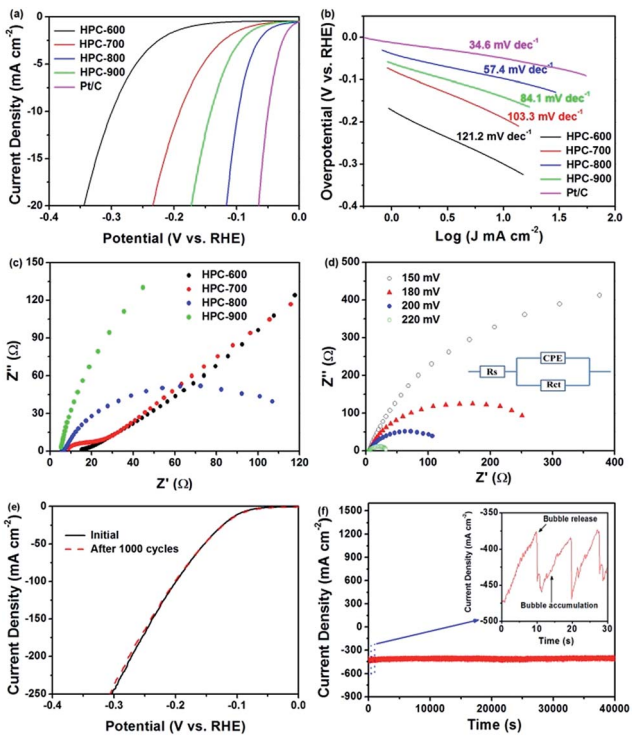

Fig. 5 (a) HER polarization curves and (b) the corresponding Tafel plots of HPC-600, HPC-700, HPC-800, HPC-900, and Pt/C, at a potential scan rate of 5 mV s^{-1} in 0.5 M H_2SO_4. (c) Electrochemical impedance spectra of the various porous carbons in HER at −0.20 V (*vs.* RHE). (d) Electrochemical impedance spectra of HPC-800 at various overpotentials (specified in figure legends) for HER in 0.5 M H_2SO_4. The inset shows the equivalent circuit where R_s is the (uncompensated) electrode series resistance, CPE is the constant-phase element and R_{ct} is the charge-transfer resistance. (e) HER polarization curves for HPC-800 before and after 1000 cycles in the stability test. (f) Time dependence of the HER current density of HPC-800 at −0.15 V *vs.* RHE, where the inset shows the impacts of bubbles formed on the electrode surface on the HER currents.

was markedly different among the series of samples. For instance, the onset potential for the HPC-800 modified electrode was only −0.012 V (*vs.* RHE), very close to that (−0.002 V) of commercial 20 wt% Pt/C at the same catalyst loading, but far more positive than those for HPC-600 (−0.186 V), HPC-700 (−0.052 V) and HPC-900 (−0.048 V). Furthermore, to reach a current density of 10 mA cm^{-2}, the required overpotential decreased in the order of HPC-600 (−0.30 V) < HPC-700 (−0.18 V) < HPC-900 (−0.15 V) < HPC-800 (−0.097 V) < Pt/C (−0.05 V). These results suggest that HPC-800 stood out as the best catalyst among the series for HER, although the performance remained somewhat subpar as compared to commercial Pt/C.

Further analysis of the HER performance was carried out with the Tafel plots. From Fig. 5b it can be seen that the Tafel slope was 57.4 mV dec^{-1} for HPC-800, much lower than those of HPC-600 (121.2 mV dec^{-1}), HPC-700 (103.3 mV dec^{-1}), and HPC-900 (84.1 mV dec^{-1}). Note that a lower Tafel slope typically suggests a more efficient HER performance. For comparison, the corresponding Tafel slope for Pt/C was 34.6 mV dec^{-1}. Mechanistically, hydrogen evolution in acid solutions on metal electrode surfaces typically involves three major reactions,[7,46,47]

$$H_3O^+ + \text{e–catalyst} \leftrightarrow \text{H–catalyst} + H_2O \text{ (Volmer reaction, Tafel slope 120 mV dec}^{-1}\text{)} \quad (1)$$

$$2\text{H–catalyst} \leftrightarrow H_2\text{–catalyst (Tafel reaction, Tafel slope 30 mV dec}^{-1}\text{)} \quad (2)$$

$$H_3O^+ + \text{e–catalyst} + \text{H–catalyst} \leftrightarrow H_2\text{–catalyst} + \text{catalyst} + H_2O \text{ (Heyrovsky reaction, Tafel slope 40 mV dec}^{-1}\text{)} \quad (3)$$

where the e–catalyst denotes metal-bound electrons, and H–catalyst and H_2–catalyst represent a hydrogen atom and a hydrogen molecule adsorbed on to a surface metal atom, respectively. Thus, the Tafel slope of 57.4 mV dec^{-1} for HPC-800 suggests that the corresponding rate-determining step most probably involved a combination of both electroreduction of protons into H* and the subsequent formation of H_2^*, that is, the Volmer–Tafel reactions.

It should be noted that such an HER performance of HPC-800 (onset potential −0.012 V, 10 mA cm^{-2} at −0.097 V *vs.* RHE, and Tafel slope 57.4 mV dec^{-1}) is markedly better than or at least comparable to those of leading Mo-based HER catalysts, such as MoS_2/reduced graphene (−0.10 V, 10 mA cm^{-2} at −0.16 V *vs.* RHE, 41 mV dec^{-1}),[47] $NiMoN_x$/C nanosheets (−0.078 V, 10 mA cm^{-2} at −0.20 V *vs.* RHE, 35.9 mV dec^{-1}),[48] defect-rich MoS_2 nanosheets (−0.12 V, 10 mA cm^{-2} at −0.18 V *vs.* RHE, 50 mV dec^{-1}),[47] WS_2 nanosheets (−0.08 V, 10 mA cm^{-2} at −0.24 V *vs.* RHE, 60 mV dec^{-1}),[49] Co-based HER catalysts such as cobalt-embedded nitrogen-rich carbon nanotubes (−0.05 V, 10 mA cm^{-2} at −0.26 V *vs.* RHE, 80 mV dec^{-1}),[50] CoS_2 nanowire arrays (−0.08 V, 10 mA cm^{-2} at −0.15 V *vs.* RHE, 51.6 mV dec^{-1}),[51] C_3N_4@N-doped graphene (−0.12 V, 10 mA cm^{-2} at −0.24 V *vs.* RHE, 51.5 mV dec^{-1}),[18] g-C_3N_4 nanoribbon–graphene (−0.08 V, 10 mA cm^{-2} at −0.2 V *vs.* RHE, 54 mV dec^{-1}),[19] and N and S co-doped nanoporous graphene (−0.14 V, 10 mA cm^{-2} at −0.39 V *vs.* RHE, 80.5 mV dec^{-1}).[20] The details are also listed in Table 1.

Electrochemical impedance spectroscopy (EIS) measurements were then carried out to further probe the electron-transfer kinetics involved. Fig. 5c depicts the Nyquist plots acquired at −0.20 V for a glass-carbon electrode modified with various porous carbons. It can be seen that the electrode series resistance (R_s) decreased in the order of 15.3 Ω for HPC-600 < 9.1 Ω for HPC-700 < 5.6 Ω for HPC-800 < 5.3 Ω for HPC-900, indicating higher electronic conductivity of the porous carbons prepared at higher pyrolysis temperature. Fig. 5d depicts the Nyquist plots of the HPC-800 modified electrode at various overpotentials, where one can see that the diameter of the semicircles, *i.e.*, the charge-transfer resistance (R_{ct}), actually diminished markedly with increasing overpotentials. More detailed analyses were carried out by fitting the impedance data to an equivalent circuit depicted in the inset of Fig. 5d, where R_s represents the (uncompensated) electrode series resistance, R_{ct} is the charge-transfer resistance and CPE is the constant-phase element. Indeed, R_{ct} decreased significantly with increasing overpotentials, from 562.3 Ω at −150 mV to 32.1 Ω at −220 mV.

In addition to excellent catalytic activity, the HPC-800 electrode also exhibited extraordinary stability in HER. Fig. 5e shows that even after 1000 continuous potential cycles, the polarization curve remained almost unchanged, suggesting long-term viability under operating conditions. To further investigate the stability of HPC-800 in HER, the current–time plots at the applied potential of −0.15 V

Table 1 Comparison of the HER activity of HPC-800 in the present study and leading literature results

HER catalysts	Onset potential (V)	Tafel slope (mV dec^{-1})	Potential at a current density of 10 mA cm^{-2} (V)	Ref.
HPC-800	−0.012	57.4	−0.10	This work
MoS_2 nanoparticles/graphene	−0.1	41	−0.16	47
Defect-rich MoS_2 nanosheets	−0.12	50	−0.18	47
$NiMoN_x$/C nanosheets	−0.078	35.9	−0.20	48
WS_2 nanosheets	−0.08	60	−0.24	49
Co-embedded N-rich carbon nanotubes	−0.05	80	−0.26	50
CoS_2 nanowire arrays	−0.08	51.6	−0.15	51
g-C_3N_4 nanoribbon–graphene	−0.08	54	−0.20	19
C_3N_4@N-doped graphene	−0.12	51.5	−0.24	18
N and S co-doped nanoporous graphene	−0.14	80.5	−0.39	20

(*vs.* RHE) is depicted in Fig. 5f. One can see that the current remains virtually invariant over 40 000 s of continuous operation. In addition, the stabilized current density (*ca.* 450 mA cm^{-2}) was even higher than that of Pt/C (*ca.* 300 mA cm^{-2}, Fig. S2†) at the same voltage. Experimentally, we also observed a number of bubbles formed on the electrode surface (video S1†), which were confirmed to be H_2 by gas chromatographic measurements. These bubbles escaped easily from the electrode surface, leading to rather periodical fluctuations of the currents, as shown in the inset of Fig. 5f. Note that the rate of hydrogen production (*ca.* 480 mmol g^{-1} h^{-1} at −0.15 V *vs.* RHE) at the HPC-800 electrode (Fig. S3†) was markedly better than leading results reported in the literature, such as three-dimensional MoS_2/graphene frameworks (358.2 mmol g^{-1} h^{-1} at −0.236 V *vs.* RHE), porous metallic MoO_2-supported MoS_2 nanosheets (120 mmol g^{-1} h^{-1} at −0.23 V *vs.* RHE) and MoS_x grown on graphene-protected 3D Ni foams (13.47 mmol g^{-1} h^{-1} at −0.2 V *vs.* RHE).[52–54]

Furthermore, the above obtained porous carbons might also serve as multifunctional catalysts with apparent electrocatalytic activity for, for instance, HER in a wide range of solution pHs (*e.g.*, 1 M KOH with pH = 14, 0.1 M phosphate buffer with pH = 7, and 0.5 M H_2SO_4 with pH = 1, Fig. S4 and S5†), oxygen evolution reaction (OER, 1 M KOH, Fig. S6†), and oxygen reduction reaction (ORR, 0.1 M KOH, Fig. S7†). The remarkable HER activity of the resulting porous carbons might be accounted for by the synergistic interactions between the N dopants and the C–S moieties[23,24] and high electrochemical area (Fig. S8†). Importantly, these catalysts might be readily prepared on a relatively large scale (Fig. S9†).

Conclusions

In this study, nitrogen and sulfur co-doped porous carbons were prepared by simple pyrolysis of human hair at elevated temperatures. The samples were thoroughly characterized by SEM, TEM, XRD, nitrogen adsorption, and Raman and X-ray photoelectron spectroscopy (XPS) measurements. Thanks to the high specific surface area and rich porosity, the nitrogen and sulfur co-doped porous carbons exhibited apparent electrocatalytic activity for HER. Among the series of samples, the porous carbon prepared by pyrolysis of human hair at 800 °C stood out as the best catalyst, with an onset potential of −0.012 V, 10 mA cm^{-2} at −0.097 V *vs.* RHE, a Tafel slope of 57.4 mV dec^{-1}, and extraordinary stability. Such performance was highly comparable to that of commercial 20 wt% Pt/C catalysts. This might be accounted for by the synergistic interactions between the N dopants and the C–S–C moieties in the graphitic skeleton that played an essential role in forming highly effective sites for HER. Overall, results from this study offer a new paradigm for the design and engineering of effective HER catalysts based on abundant biowastes, in particular, in light of the multifunctional applications of the nitrogen and sulfur co-doped porous carbons from human hair in, for instance, HER in a wide range of pH, OER, and ORR.

Acknowledgements

This work was supported by the National Recruitment Program of Global Experts, the PhD Start-up Funds of the Natural Science Foundation of Guangdong Province (S2013040016465), and Zhujiang New Stars of Science & Technology (2014J2200061).

Notes and references

1 R. Subbaraman, D. Tripkovic, D. Strmcnik, K.-C. Chang, M. Uchimura, A. P. Paulikas, V. Stamenkovic and N. M. Markovic, *Science*, 2011, **334**, 1256–1260.
2 W. Zhou, X.-J. Wu, X. Cao, X. Huang, C. Tan, J. Tian, H. Liu, J. Wang and H. Zhang, *Energy Environ. Sci.*, 2013, **6**, 2921–2924.
3 I. E. L. Stephens and I. Chorkendorff, *Angew. Chem., Int. Ed.*, 2011, **50**, 1476–1477.
4 W. Zhou, K. Zhou, D. Hou, X. Liu, G. Li, Y. Sang, H. Liu, L. Li and S. Chen, *ACS Appl. Mater. Interfaces*, 2014, **6**, 21534–21540.
5 H. Vrubel and X. Hu, *Angew. Chem.*, 2012, **124**, 12875–12878.
6 C. Wan, B. M. Regmi Yn Fau-Leonard and B. M. Leonard, *Angew. Chem., Int. Ed.*, 2014, **53**, 6407–6410.
7 W. Zhou, D. Hou, Y. Sang, S. Yao, J. Zhou, G. Li, L. Li, H. Liu and S. Chen, *J. Mater. Chem. A*, 2014, **2**, 11358–11364.
8 Y.-H. Chang, C.-T. Lin, T.-Y. Chen, C.-L. Hsu, Y.-H. Lee, W. Zhang, K.-H. Wei and L.-J. Li, *Adv. Mater.*, 2013, **25**, 756–760.
9 J. Xie, J. Zhang, S. Li, F. Grote, X. Zhang, H. Zhang, R. Wang, Y. Lei, B. Pan and Y. Xie, *J. Am. Chem. Soc.*, 2013, **135**, 17881–17888.
10 Z. Huang, Z. Chen, Z. Chen, C. Lv, H. Meng and C. Zhang, *ACS Nano*, 2014, **8**, 8121–8129.
11 E. J. Popczun, C. G. Read, C. W. Roske, N. S. Lewis and R. E. Schaak, *Angew. Chem., Int. Ed.*, 2014, **53**, 5427–5430.
12 E. J. Popczun, J. R. McKone, C. G. Read, A. J. Biacchi, A. M. Wiltrout, N. S. Lewis and R. E. Schaak, *J. Am. Chem. Soc.*, 2013, **135**, 9267–9270.
13 D. Kong, H. Wang, Z. Lu and Y. Cui, *J. Am. Chem. Soc.*, 2014, **136**, 4897–4900.
14 X. Zou, X. Huang, A. Goswami, R. Silva, B. R. Sathe, E. Mikmeková and T. Asefa, *Angew. Chem.*, 2014, **53**, 4372–4376.
15 J. Deng, P. Ren, D. Deng, L. Yu, F. Yang and X. Bao, *Energy Environ. Sci.*, 2014, **7**, 1919–1923.
16 W. Zhou, Y. Zhou, L. Yang, J. Huang, Y. Ke, K. Zhou, L. Li and S. Chen, *J. Mater. Chem. A*, 2015, **3**, 1915–1919.
17 W. Zhou, J. Zhou, Y. Zhou, J. Lu, K. Zhou, L. Yang, Z. Tang, L. Li and S. Chen, *Chem. Mater.*, 2015, **27**, 2026–2032.
18 Y. Zheng, Y. Jiao, Y. Zhu, L. H. Li, Y. Han, Y. Chen, A. Du, M. Jaroniec and S. Z. Qiao, *Nat. Commun.*, 2014, **5**, 3783.
19 X. Huang, Y. Zhao, Z. Ao and G. Wang, *Sci. Rep.*, 2014, **4**, 7557.
20 Y. Ito, W. Cong, T. Fujita, Z. Tang and M. Chen, *Angew. Chem., Int. Ed.*, 2014, **126**, 1–7.

21 R. K. Das, Y. Wang, S. V. Vasilyeva, E. Donoghue, I. Pucher, G. Kamenov, H.-P. Cheng and A. G. Rinzler, *ACS Nano*, 2014, **8**, 8447–8456.
22 W. Cui, Q. Liu, N. Cheng, A. M. Asiri and X. Sun, *Chem. Commun.*, 2014, **50**, 9340–9342.
23 Y. Liu, H. Yu, X. Quan, S. Chen, H. Zhao and Y. Zhang, *Sci. Rep.*, 2014, **4**, 6843.
24 W. Wei, H. Liang, K. Parvez, X. Zhuang, X. Feng and K. Müllen, *Angew. Chem., Int. Ed.*, 2014, **53**, 1570–1574.
25 Y. Zheng, Y. Jiao, L. H. Li, T. Xing, Y. Chen, M. Jaroniec and S. Z. Qiao, *ACS Nano*, 2014, **8**, 5290–5296.
26 S. Gao, Y. Chen, H. Fan, X. Wei, C. Hu, H. Luo and L. Qu, *J. Mater. Chem. A*, 2014, **2**, 3317–3324.
27 J. Zhang, S. Wu, X. Chen, K. Cheng, M. Pan and S. Mu, *RSC Adv.*, 2014, **4**, 32811–32816.
28 K. Zhou, W. Zhou, X. Liu, Y. Wang, J. Wan and S. Chen, *ACS Appl. Mater. Interfaces*, 2014, **6**, 14911–14918.
29 W. Qian, F. Sun, Y. Xu, L. Qiu, C. Liu, S. Wang and F. Yan, *Energy Environ. Sci.*, 2014, **7**, 379–386.
30 W. Ding, Z. Wei, S. Chen, X. Qi, T. Yang, J. Hu, D. Wang, L.-J. Wan, S. F. Alvi and L. Li, *Angew. Chem., Int. Ed.*, 2013, **52**, 11755–11759.
31 K. N. Chaudhari, M. Y. Song and J.-S. Yu, *Small*, 2014, **10**, 2625–2636.
32 F. Cesano, M. M. Rahman, S. Bertarione, J. G. Vitillo, D. Scarano and A. Zecchina, *Carbon*, 2012, **50**, 2047–2051.
33 L. Sun, C. Tian, M. Li, X. Meng, L. Wang, R. Wang, J. Yin and H. Fu, *J. Mater. Chem. A*, 2013, **1**, 6462–6470.
34 M. Sevilla, R. Mokaya and A. B. Fuertes, *Energy Environ. Sci.*, 2011, **4**, 2930–2936.
35 L. Qie, W.-M. Chen, Z.-H. Wang, Q.-G. Shao, X. Li, L.-X. Yuan, X.-L. Hu, W.-X. Zhang and Y.-H. Huang, *Adv. Mater.*, 2012, **24**, 2047–2050.
36 S. Gao, K. Geng, H. Liu, X. Wei, M. Zhang, P. Wang and J. Wang, *Energy Environ. Sci.*, 2015, **8**, 221–229.
37 P. K. Chu and L. Li, *Mater. Chem. Phys.*, 2006, **96**, 253–277.
38 H. Zhong, C. Deng, Y. Qiu, L. Yao and H. Zhang, *J. Mater. Chem. A*, 2014, **2**, 17047–17057.
39 J. Zhao, F. Cheng, C. Yi, J. Liang, Z. Tao and J. Chen, *J. Mater. Chem.*, 2009, **19**, 4108–4116.
40 H. Zhong, H. Zhang, S. Liu, C. Deng and M. Wang, *ChemSusChem*, 2013, **6**, 807–812.
41 G. Wu, C. M. Johnston, N. H. Mack, K. Artyushkova, M. Ferrandon, M. Nelson, J. S. Lezama-Pacheco, S. D. Conradson, K. L. More, D. J. Myers and P. Zelenay, *J. Mater. Chem.*, 2011, **21**, 11392–11405.
42 S. Kundu, T. C. Nagaiah, W. Xia, Y. Wang, S. V. Dommele, J. H. Bitter, M. Santa, G. Grundmeier, M. Bron, W. Schuhmann and M. Muhler, *J. Phys. Chem. C*, 2009, **113**, 14302–14310.
43 X. a. Chen, X. Chen, X. Xu, Z. Yang, Z. Liu, L. Zhang, X. Xu, Y. Chen and S. Huang, *Nanoscale*, 2014, **6**, 13740–13747.
44 Z. Yang, Z. Yao, G. Li, G. Fang, H. Nie, Z. Liu, X. Zhou, X. a. Chen and S. Huang, *ACS Nano*, 2011, **6**, 205–211.
45 J.-e. Park, Y. J. Jang, Y. J. Kim, M.-s. Song, S. Yoon, D. H. Kim and S.-J. Kim, *Phys. Chem. Chem. Phys.*, 2014, **16**, 103–109.
46 J. G. N. Thomas, *Trans. Faraday Soc.*, 1961, **57**, 1603–1611.
47 Y. Li, H. Wang, L. Xie, Y. Liang, G. Hong and H. Dai, *J. Am. Chem. Soc.*, 2011, **133**, 7296–7299.
48 W. F. Chen, K. Sasaki, C. Ma, A. I. Frenkel, N. Marinkovic, J. T. Muckerman, Y. Zhu and R. R. Adzic, *Angew. Chem., Int. Ed.*, 2012, **51**, 6131–6135.
49 D. Voiry, H. Yamaguchi, J. Li, R. Silva, D. C. B. Alves, T. Fujita, M. Chen, T. Asefa, V. B. Shenoy, G. Eda and M. Chhowalla, *Nat. Mater.*, 2013, **12**, 850–855.
50 X. Zou, X. Huang, A. Goswami, R. Silva, B. R. Sathe, E. Mikmeková and T. Asefa, *Angew. Chem., Int. Ed.*, 2014, **53**, 4372–4376.
51 M. S. Faber, R. Dziedzic, M. A. Lukowski, N. S. Kaiser, Q. Ding and S. Jin, *J. Am. Chem. Soc.*, 2014, **136**, 10053–10061.
52 L. Yang, W. Zhou, D. Hou, K. Zhou, G. Li, Z. Tang, L. Li and S. Chen, *Nanoscale*, 2015, **7**, 5203–5208.
53 Y.-H. Chang, C.-T. Lin, T.-Y. Chen, C.-L. Hsu, Y.-H. Lee, W. Zhang, K.-H. Wei and L.-J. Li, *Adv. Mater.*, 2013, **25**, 755.
54 W. Zhou, K. Zhou, D. Hou, X. Liu, G. Li, Y. Sang, H. Liu, L. Li and S. Chen, *ACS Appl. Mater. Interfaces*, 2014, **6**, 21534–21540.